Fast estimation of reaction rates in spherical and non-spherical porous catalysts

John P. Wakefield[a,*], Aaron M. Lattanzi[b], M. Brennan Pecha[d], Peter N. Ciesielski[d], Jesse Capecelatro[b,c]

[a] *University of Michigan, Department of Mathematics*
[b] *University of Michigan, Department of Mechanical Engineering*
[c] *University of Michigan, Department of Aerospace Engineering*
[d] *National Renewable Energy Laboratory*

Abstract

We present a methodology for modeling multi-step reaction rates in porous catalyst particles for use in CFD–DEM and two fluid models. Single-step effectiveness factors based on a Thiele modulus, while useful, cannot accurately capture the cascading reaction systems common in high temperature vapor-phase chemical reactors like fluidized catalytic cracking units and catalytic biomass fast pyrolysis systems. Instead, multi-step effectiveness vectors derived from steady-state solutions to the governing reaction-diffusion equations are needed. Solutions for various catalyst shapes are presented, including spheres, cylinders, and prisms. Computational challenges inherent in repeated evaluation of reaction rates with diffusion limitations are discussed, and an efficient implementation based on pre-computed lookup tables is proposed and demonstrated on a simulation of a fluidized bed reactor. Open-source code is provided for the compilation of reaction rate tables for use in ODE, DEM, and two-fluid models.

Keywords: intraparticle diffusion, effectiveness factor, lumped kinetics, catalysis, non-spherical

1. Introduction

Many industrial processes involve heterogeneous chemical reactions between a fluid and a solid surface. Of particular interest are fluidized bed reactors, in which large numbers of small catalyst or fuel particles are present. These particles are typically porous to increase catalyst availability. However, accurately modeling reaction rates within porous catalysts is challenging. When considering reacting systems at industrial scale, resolution at the molecular or pore scale is not computationally feasible. Instead, mean (i.e. 'effective') reaction rates must be used.

Previous works have modeled reactors with gas-solid interactions consisting of a single reaction limited by diffusion within particles [1, 2, 3] and multiple reactions without diffusion limitations [4, 5, 6, 7]. For a single-stage reaction, an effectiveness factor is defined as the ratio of actual reaction rate integrated over the particle to the reaction rate without diffusion limitations integrated over the particle; $\int_\Omega \dot{r}\ \mathrm{d}V = \eta^p\, V_p\, \dot{r}^{\mathrm{nom}}$ where $\dot{r}^{\mathrm{nom}}$ is the reaction rate without diffusion limitations, $\dot{r}$ is the actual reaction rate inside the particle, Ω is the set of points within the boundary of the superficial particle, and V_p is the volume of the particle. Solutions to scalar diffusion limited processes inside non-spherical geometries and resulting effectiveness factors have also been explored previously [8, 9]. Zhu et al. [10] showed accurate effective multi-stage reaction rates are important for matching experimental data.

Wei [11] proposed diagonalization for decoupling systems of irreversible first-order reactions. This was revisited by Lattanzi et al. [12], who introduced the multi-stage effectiveness vector (MEV), a vector $\boldsymbol{\eta}^p$ of effectiveness factors η_i^p such that $\int_\Omega \dot{r}_{ij}\ \mathrm{d}V = \eta_i^p\, V_p\, \dot{r}^{\mathrm{nom}}$ where $\dot{r}_{ij}$ is the observed rate of mass conversion from species i to species j and $\dot{r}_{ij}^{\mathrm{nom}}$ is the same rate without diffusion limitations. The dependence of the factor η_i^p only upon the source species is a consequence of the first order assumption. The present work discusses the limitations of this approach with respect to Biot number, the possible extensions of this approach, and, most importantly, the practicality of utlizing this approach to estimate rate constants in simulations of fluidized bed reactors under the pseudo-steady state assumption.

We present a general 'recipe' for the computation of first order multistage reactions by reducing them to combinations of single-stage reactions (Sec. 2.1). We extend the work of Wei [11] and Lattanzi et al. [12] to enable practical implementation in reactor-scale codes. Catalyst geometry may introduce complexity into the estimation of single-stage reaction rates, but does not affect the construction of multi-stage rates from single-stage rates. Section 3 discusses the efficiency of some effectiveness factor forms in the context of computational fluid dynamics (CFD) discrete element modeling (DEM) in which enormous numbers of reaction rate evaluations are required. Efficient calculation of corrected reaction rates based upon pre-compiled tables is proposed (Sec. 2.2) and utilized in a proof of concept CFD–DEM computation of catalysis

*Corresponding author
Email address: jwake@umich.edu (John P. Wakefield)

in a fluidized bed (Sec. 4). The pre-processing computations for arbitrary first-order chemistry are open-source and made available to aid in the implementation of the approach described here to reactor-scale simulation methodologies like CFD–DEM and two-fluid models.

The approach presented herein applies to any number of reaction stages and allows for decreased reaction rates due to environmental factors, e.g. coking on catalyst particles in fluidized catalytic cracking (FCC). Though the present discussion has general applicability to coupled and reversible kinetics, the primary focus of this work pertains to modeling of fluidized catalytic systems (e.g., [1, 7]) in which reactions are irreversible. However, reversible reactions can be modeled using this framework under certain conditions. The primary limitation of this approach is a harsh restriction on applicable boundary conditions (Appendix A).

2. The Multistage Problem

As a fundamental modeling assumption we split the domain into two parts: one inside the superficial volume of the catalyst particle and one entirely within the fluid phase. Points 'inside the catalyst' are points at which advection becomes negligible due to the small dimension of the pores. In this section we will focus on the regions 'inside' the catalyst particles. Careful consideration of the outer surface of the superficial pellet and models of the fluid boundary layer remain an area for future research. Let N_r be the number of gaseous reactants, N_p be the number of (not necessarily gaseous) products, and $N = N_r + N_p$ be the total number of species. Index reacting species such that $1 \le i \le N_r$ and $N_r{+}1 = N{-}N_p \le i \le N$ are strictly products (i.e., not a reactant in any reaction). The rate constant for conversion of species i to species j is denoted k_{ij}. The constraint that solid species may not react results in $k_{ij} = 0$ for all $N_r{+}1 = N{-}N_p{+}1 \le i \le N$.

Gaseous species within the porous catalyst are governed by

$$\begin{aligned}\frac{\partial(\epsilon\rho_g Y_i)}{\partial t} + \nabla\cdot(\boldsymbol{u}\,\epsilon\rho_g Y_i) =& \nabla\cdot\underbrace{(\epsilon\rho_g \mathcal{D}_i \nabla Y_i)}_{\boldsymbol{J}_i} \\ &- \sum_{j=1}^{N} \underbrace{\psi k_{ij}\epsilon\rho_g Y_i}_{\dot{r}_{ij}} \\ &+ \sum_{j=1}^{N} \underbrace{\psi k_{ji}\epsilon\rho_g Y_j}_{\dot{r}_{im}}\end{aligned} \tag{1}$$

where $1 \le i \le N_r$, ρ_g is the gas phase density, ϵ is the particle voidage, Y_i is the mass fraction of species i, $\mathcal{D}_i$ is the (effective) diffusion coefficient of the i-th species, and ψ is deactivation factor due to other phenomena (e.g., coking).

Let $\bar{\mathcal{D}}_i$ be the effective diffusivity of species i within the particle, L be a characteristic length scale, T be a a characteristic time, and let $T\hat{t} = t$ to obtain nondimensionalized equations

$$\begin{aligned}\left(\frac{L^2}{T\bar{\mathcal{D}}_i}\right)\frac{\partial(\hat{\rho}_g Y_i)}{\partial \hat{t}} + \mathrm{Pe}_i\,\hat{\nabla}\cdot(\hat{\boldsymbol{u}}\,(\hat{\rho}_g Y_i)) =& \hat{\nabla}\cdot\left(\hat{\rho}_g\hat{\mathcal{D}}_i\hat{\nabla}(Y_i)\right) \\ &- \hat{\rho}_g\underbrace{\left(\sum_{j=1}^{N}\frac{\psi k_{ij}L^2}{\bar{\mathcal{D}}_i}\right)}_{\phi_i^2} Y_i \\ &+ \hat{\rho}_g\sum_{j=1}^{N}\underbrace{\left(\frac{\psi k_{ji}L^2}{\bar{\mathcal{D}}_i}\right)}_{\phi_{ij}^2} Y_j\end{aligned} \tag{2}$$

where the Péclet number is $\mathrm{Pe}_i = \bar{u}L/(T\bar{\mathcal{D}}_i)$ and nondimensional fluid quantities are $\hat{\boldsymbol{u}} = \boldsymbol{u}/\bar{u}$, $\hat{\rho}_g = \epsilon\rho_g/\overline{\epsilon\rho_g}$, and $\hat{\mathcal{D}}_i = \mathcal{D}_i/\bar{\mathcal{D}}_i$. Assume $\bar{u}$ and $\bar{\mathcal{D}}_i$ are chosen such that $\hat{\boldsymbol{u}}$ and $\hat{\mathcal{D}}_i$ are order one. If we take the convective term to be small, $\mathcal{D}_i$ is constant in space ($\hat{\mathcal{D}}_i = 1$), density variations are small throughout the particle ($\hat{\rho}_g \approx 1$), and consider the steady state problem we obtain

$$-\hat{\nabla}^2 Y_i + \phi_i^2 Y_i - \sum_{j=1}^{N}\phi_{ij}^2 Y_j = 0. \tag{3}$$

The concentration of the i-th species is $C_i = \epsilon\rho_g Y_i/W_i$, allowing us to rewrite Eq. (3) in terms of concentration as

$$-\hat{\nabla}^2 C_i + \phi_i^2 C_i - \sum_{j=1}^{N}\phi_{ij}^2\frac{W_j}{W_i}C_j = 0, \tag{4}$$

where we have assumed that deviations in $\epsilon\rho_g$ are negligible throughout the particle. Effective diffusion within the particle will be modeled by Knudsen diffusion [13, 14]

$$\mathcal{D}_i = \frac{D_{\mathrm{pore}}}{3}\sqrt{\frac{8\mathcal{R}T}{\pi W_i}}\,\frac{\epsilon}{\tau}. \tag{5}$$

We will solve in terms of mass fraction (Eq. (3)) as it more obviously conserves mass and is consistent with typical implementatons in CFD codes.

For the boundary condition, we assume Fick's law holds at the interior edge of the catalyst particle, yielding the mass flux $\boldsymbol{j}_i^{\mathrm{int}} = -\mathcal{D}_i(\epsilon\rho_g\nabla Y_i)$. The mass flux from the solid to the free stream can be approximated by $\boldsymbol{j}_i^{\mathrm{ext}}\cdot\mathbf{n} = \epsilon\rho_g\,k_c\,(Y_i - Y_{i,\infty})$ where k_c is a mass transfer coefficient, $Y_{i,\infty}$ is the free stream concentration of the i-th species, and $\mathbf{n}$ is a unit normal vector [15]. The resulting boundary condition is obtained by setting $\boldsymbol{j}_i^{\mathrm{int}} = \boldsymbol{j}_i^{\mathrm{ext}}$,

$$\frac{1}{\mathrm{Bi}_i}\hat{\nabla}Y_i\cdot\mathbf{n} + Y_i = Y_{i,\infty}. \tag{6}$$

$\mathrm{Bi} = k_c L/\mathcal{D}_i$ is the mass transfer Biot number. It will ultimately be required $\mathrm{Bi} = \mathrm{Bi}_1 = \mathrm{Bi}_2 = \cdots = \mathrm{Bi}_{N_r}$; the reason for this condition is discussed in Appendix A.

Symbol	Description
B	reaction rate transform for all species
B_g	reaction rate transform for gaseous species
B_s	reaction rate transform for solid species
b_{ij}	entries of B, B_g
Bi_i	Biot number for species i
Bi	Biot number for all species
C_i	concentration of i-th species
$\mathcal{D}_i$	effective scalar diffusion coefficient of species i
D_{pore}	catalyst particle pore diameter
ϵ	catalyst particle voidage
ϕ_i^2 and ϕ_{ij}^2	Thiele moduli
$\boldsymbol{\eta}^p$	multistep effectiveness vector
η_i^p	effectiveness factor for species i in particle p
$\eta(\lambda, \mathrm{Bi})$	single-stage effectiveness factor
$H(\boldsymbol{\lambda}, \mathrm{Bi})$	$\mathrm{Diag}_i(\eta(\lambda_i, \mathrm{Bi}))$
$\boldsymbol{j}_i^{\mathrm{int}}$	mass flux of species i inside superficial particle
$\boldsymbol{j}_i^{\mathrm{ext}}$	mass flux of species i to particle boundary
k_c	mass transfer coefficient at particle boundary
k_{ij}	reaction rate constant (species i to species j)
L	nondimensionalization length
λ_k	kth eigenvalue of B
Λ	$\mathrm{Diag}_k(\lambda_k)$
N_r	number of reacting gaseous species
N_p	number of product species
N	total number of species ($N = N_r + N_p$)
Ω	superficial particle domain
Pe_i	Péclet number for i-th species
ψ	deactivation due to coking
$\mathcal{R}$	ideal gas constant
R	matrix of eigenvectors of B
$\dot{r}_{ij}$	actual effective reaction rate (species i to j)
$\dot{r}_{ij}^{\mathrm{nom}}$	nominal reaction rate
ρ_g	gas density
T	nondimensional time
τ	catalyst particle tortuosity
$\boldsymbol{u}$	fluid velocity
V_p	volume of particle p
W_i	molecular weight of i-th species
W	mixture molecular weight
Y_i	mass fraction of species i
$Y_{i,\infty}$	mass fraction of species i in free stream
$\boldsymbol{Y}_\infty$	vector of $Y_{i,\infty}$
$\hat{\boldsymbol{Y}}$	transformed mass fractions $\hat{\boldsymbol{Y}} = R^{-1}\boldsymbol{Y}$
$\hat{Y}_k$	kth entry of $\hat{\boldsymbol{Y}}$

(a) List of symbols used in computation of effectiveness factors.

Symbol	Description
A_{ij}	pre-exponential factor (Eq. (50))
$\boldsymbol{C}$	force of collisions
d_p	particle diameter
$\mathcal{D}_{g,i}$	gas-phase diffusivity of species i
ε_g	gaseous volume fraction
Ea_{ij}	activation energy (Eq. (50))
$\boldsymbol{f}_p^{\mathrm{drag}}$	force of drag on particle
$\mathcal{F}$	force between particles and fluid
$\boldsymbol{g}$	acceleration due to gravity
$\mathcal{G}$	smoothing kernel
m_p	particle mass
m_p^{CA}	mass of uncoked particle
m_p^{CK}	mass of coke on particle
$\mathcal{M}_i$	mass source/sink for species i
μ_g	dynamic viscosity
P_g	static pressure
p_g	pressure
$\boldsymbol{\tau}_g$	fluid stress tensor
T_g	gas temperature
T_0	reference temperature (Eq. (50))
$\boldsymbol{u}_g$	fluid velocity
$\boldsymbol{u}_{g@p}$	$\boldsymbol{u}$ evaluated at particle p
$Y_{g,i}$	gas phase mass fraction of species i

(b) List of symbols used in CFD–DEM (Sec. 4).

Table 1: List of symbols.

2.1. Reduction of the Multi-Stage Problem

The reaction rates coupling the systems in Eqs. (2) and (3) are of the form $-B_g\boldsymbol{Y}$ where $B_g \in \mathbb{R}^{N_r \times N_r}$ contains entries $b_{ij} = \delta_{ij}\phi_i^2 - \phi_{ij}^2$. In what follows we will diagonalize the matrix B_g, thus obtaining decoupled equations in an alternative coordinate system. Omitting hats for ease of notation, Eq. (3) becomes, for $i \in \{1, 2, \ldots, N_r\}$,

$$\begin{aligned} -\nabla^2 Y_i + \boldsymbol{b}_i \cdot \boldsymbol{Y} &= 0 \qquad \text{in } \hat{\Omega} \\ \frac{1}{\mathrm{Bi}_i}\nabla Y_i \cdot \mathbf{n} + Y_i &= Y_{i,\infty} \quad \text{on } \partial\hat{\Omega} \end{aligned} \tag{7}$$

where $\boldsymbol{b}_i$ is the i-th row of the matrix B_g. Letting $B_g R = R\Lambda$ be an eigendecomposition of B_g where $\Lambda_{ij} = \delta_{ij}\lambda_i$ and $\boldsymbol{Y} = R\hat{\boldsymbol{Y}}$, where entries $\hat{Y}_k$ of $\hat{\boldsymbol{Y}}$ are functions of $\boldsymbol{x}$, Eq. (7) becomes

$$\begin{aligned} 0 &= -\nabla^2 R\hat{\boldsymbol{Y}} + B_g R\hat{\boldsymbol{Y}} \\ &= -\nabla^2 R\hat{\boldsymbol{Y}} + R\Lambda\hat{\boldsymbol{Y}} \\ &= R\left(-\nabla^2\hat{\boldsymbol{Y}} + \Lambda\hat{\boldsymbol{Y}}\right). \end{aligned}$$

Because R is invertible,

$$-\nabla^2\hat{Y}_k + \lambda_k\hat{Y}_k = 0 \tag{8}$$

for each k. Similarly, letting Bi be the matrix with entries $\mathrm{Bi}_{ij} = \delta_{ij}\mathrm{Bi}_i$, for the boundary conditions yields

$$\mathrm{Bi}^{-1}\nabla\boldsymbol{Y}\cdot\mathbf{n} + \boldsymbol{Y} = \mathrm{Bi}^{-1}\nabla(R\hat{\boldsymbol{Y}})\cdot\mathbf{n} + R\hat{\boldsymbol{Y}} = \boldsymbol{Y}_\infty$$

where $\boldsymbol{Y}_\infty$ is a vector with entries $Y_{i,\infty}$. Because R is linear operator and constant throughout the particle,

$$R^{-1}\mathrm{Bi}^{-1}R\left(\nabla\hat{\boldsymbol{Y}}\cdot\mathbf{n}\right) + \hat{\boldsymbol{Y}} = R^{-1}\boldsymbol{Y}_\infty. \tag{9}$$

From Eq. (9) we observe that diagonalization only truly decouples the equations if $R^{-1}\mathrm{Bi}^{-1}R$ is a diagonal matrix, which is only the case if the Biot number is the same for all species. A more thorough discussion of why this approach is not readily applicable to the case of differing Biot numbers is shown in Appendix A. From this point forward we will make the assumption that Biot numbers are the same for all species, allowing us to write Eq. (9) as

$$\frac{1}{\mathrm{Bi}}(\nabla\hat{Y}_k\cdot\mathbf{n}) + \hat{Y}_k = (R^{-1}\boldsymbol{Y}_\infty)_k. \tag{10}$$

To obtain formulas for effective reaction rates, first let $K \in \mathbb{R}^{N_r \times N}$ be the matrix consisting of rate constants

$$K = \begin{bmatrix} k_{11} & k_{12} & \cdots & k_{1N} \\ k_{21} & k_{22} & \cdots & k_{2N} \\ \vdots & \vdots & \ddots & \vdots \\ k_{N_r 1} & k_{N_r 2} & \cdots & k_{N_r N} \end{bmatrix}. \tag{11}$$

We choose arbitrary $\bar{\mathcal{D}}_i \neq 0$ for species $i > N_r$ in order to obtain a non-dimensional time for the strictly product species. In a manner similar to Eq. (2) we define ϕ_i^2 and ϕ_{ij}^2 for strictly product species as well. Then

$$\psi\left(\mathrm{Diag}(\boldsymbol{Y})K\mathbf{1} - K^T\boldsymbol{Y}\right) = \frac{1}{L^2}DB\boldsymbol{Y},$$

where

$$B = \begin{bmatrix} B_g \\ B_s \end{bmatrix} \in \mathbb{R}^{N\times N_r}$$

has entries $b_{ij} = \phi_i^2\delta_{ij} - \phi_{ij}^2$ and D is the diagonal matrix with entries $\bar{\mathcal{D}}_i$ on the diagonal. (We use the notation $\mathrm{Diag}_m(a_m)$ to mean the $M \times M$ square matrix with entries $a_1, a_2, \ldots, a_M$ on the diagonal and zeros elsewhere.) The first N_g rows of B correspond to the consumption of gaseous reactants; let $B_s \in \mathbb{R}^{N_p \times N_r}$ be the matrix containing rows $N_r + 1$ through N of B. The rates at which species are created in the catalyst particle are entries M_i^p of the vector $\boldsymbol{M}_i^p$:

$$\begin{aligned} \boldsymbol{M}^p &= \int_\Omega \epsilon\rho_g\psi\left(-\mathrm{Diag}(\boldsymbol{Y})K\mathbf{1} + K^T\boldsymbol{Y}\right)\,\mathrm{d}V \\ &= \frac{1}{L^2}\,\epsilon\rho_g DB\int_\Omega \boldsymbol{Y}\,\mathrm{d}V \qquad (12) \\ &= \frac{1}{L^2}\,\epsilon\rho_g DBR\int_\Omega \hat{\boldsymbol{Y}}\,\mathrm{d}V. \qquad (13) \end{aligned}$$

For conservative reactions, $\mathbf{1}^T DB = \mathbf{0}^T$. The vector $\boldsymbol{M}^p$ can be constructed entirely from the values $\int_\Omega \hat{Y}_i\,\mathrm{d}V$ for $1 \le i \le N_r$. For irreversible reactions, B_g is a lower triangular matrix; the eigenvalues are then on the diagonal, and eigenvectors can be found by simple substitution. We will proceed to outline how this can be computed numerically (Sec. 2.2) and how these single-step solutions can be found for a variety of shapes (Sec. 3).

2.2. Numerical Solutions

Because we can construct effective reaction rates from the integrals of our new coordinates over the particle, we can turn our attention to computing these quickly. The approach taken here is to construct a table of reference solutions that can be interpolated to approximate the required quantities. Let $\hat{Z}^{(\lambda,\mathrm{Bi})}$ represent a reference solution corresponding to constants λ and Bi, i.e.

$$-\nabla^2\hat{Z}^{(\lambda,\mathrm{Bi})} + \lambda\hat{Z}^{(\lambda,\mathrm{Bi})} = 0 \qquad \text{in } \hat{\Omega} \tag{14a}$$

$$\frac{1}{\mathrm{Bi}}\nabla\hat{Z}^{(\lambda,\mathrm{Bi})}\cdot\mathbf{n} + \hat{Z}^{(\lambda,\mathrm{Bi})} = 1 \qquad \text{on } \partial\hat{\Omega}. \tag{14b}$$

First, observe that this is a linear partial differential equation (PDE); if $\hat{Z}^{(\lambda,\mathrm{Bi})}$ satisfies Eq. (14) then

$$-\nabla^2(\alpha\hat{Z}^{(\lambda,\mathrm{Bi})}) + \lambda(\alpha\hat{Z}^{(\lambda,\mathrm{Bi})}) = 0 \qquad \text{in } \hat{\Omega} \tag{15a}$$

$$\frac{1}{\mathrm{Bi}}\nabla(\alpha\hat{Z}^{(\lambda,\mathrm{Bi})})\cdot\mathbf{n} + (\alpha\hat{Z}^{(\lambda,\mathrm{Bi})}) = \alpha \quad \text{on } \partial\hat{\Omega}. \tag{15b}$$

In light of this, let $\hat{Y}_k = \alpha_k\hat{Z}^{(\lambda_k,\mathrm{Bi})}$. Because $\hat{Y}_k$ satisfies Eq. (8) the desired PDE is satisfied in the interior of the

domain. To ensure the correct boundary condition we need to satisfy Eq. (10), thus

$$\begin{aligned}\frac{1}{\mathrm{Bi}}(\nabla\hat{Y}_k\cdot\mathbf{n})+\hat{Y}_k &= \frac{1}{\mathrm{Bi}}(\nabla(\alpha_k\hat{Z}^{(\lambda_k,\mathrm{Bi})})\cdot\mathbf{n})+\alpha_k\hat{Z}^{(\lambda_k,\mathrm{Bi})}\\ &= \alpha_k\underbrace{\left(\frac{1}{\mathrm{Bi}}\nabla\hat{Z}^{(\lambda_k,\mathrm{Bi})}\cdot\mathbf{n}+\hat{Z}^{(\lambda_k,\mathrm{Bi})}\right)}_{1}\\ &= (R^{-1}\boldsymbol{Y}_\infty)_k. \end{aligned} \tag{16}$$

Pointwise solutions are then

$$Y_i(\boldsymbol{x}) = \sum_k r_{i,p}\,\underbrace{(R^{-1}\boldsymbol{Y}_\infty)_k}_{\alpha_k}\,\hat{Z}^{(\lambda_k,\mathrm{Bi})}(\boldsymbol{x}) \tag{17}$$

or in matrix form

$$\boldsymbol{Y}(\boldsymbol{x}) = R\,\mathrm{Diag}_k(\hat{\boldsymbol{Z}}^{(\lambda_k,\mathrm{Bi})}(\boldsymbol{x}))\,\boldsymbol{\alpha}, \tag{18}$$

where α_k is the k-th entry of $\boldsymbol{\alpha}$. For effectiveness factors we need the integral of Y_i over $\hat{\Omega}$; these are

$$\begin{aligned}\int_{\hat{\Omega}} Y_i\,\mathrm{d}V &= \sum_k r_{i,p}\,\alpha_k\int_{\hat{\Omega}}\hat{Z}^{(\lambda_k,\mathrm{Bi})}\,\mathrm{d}V\\ &= \left(R\,\mathrm{Diag}_k\left(V_p\,\eta(\lambda_k,\mathrm{Bi})\right)\,R^{-1}\boldsymbol{Y}_\infty\right)_i, \end{aligned} \tag{19}$$

where

$$\eta(\lambda_k,\mathrm{Bi}) = \frac{1}{V_p}\int_{\hat{\Omega}}\hat{Z}^{(\lambda_k,\mathrm{Bi})}\,\mathrm{d}V \tag{20}$$

are single stage effectiveness factors. Combining Eq. (13) with Eq. (19) yields

$$\frac{\boldsymbol{M}^p}{\epsilon\rho_g V_p} = \underbrace{\frac{1}{L^2}\mathrm{Diag}_i\left(\bar{\mathcal{D}}_i\right)BR\,\mathrm{Diag}_k\left(\eta(\lambda_k,\mathrm{Bi})\right)R^{-1}}_{\text{an } N\times N_r \text{ matrix that depends on } T \text{ and } \psi}\boldsymbol{Y}_\infty \tag{21a}$$

$$= \frac{\mathrm{Diag}_i(\bar{\mathcal{D}}_i)}{L^2}\begin{bmatrix} R\Lambda \\ B_sR\end{bmatrix}\mathrm{Diag}_k\left(\eta(\lambda_k,\mathrm{Bi})\right)R^{-1}\boldsymbol{Y}_\infty, \tag{21b}$$

where we note that the last line depends only on $\bar{\mathcal{D}}_i/L^2$, R, Λ, B_s, and the integrals of effectiveness factors. The 'diffusion coefficients' $\bar{\mathcal{D}}_i$ (arbitrary constants for solids), matrix R, vector of eigenvalues, and matrix B_s comprise in total $N+(N+1)\,N_r$ scalars.

There are no restrictions upon how $\hat{Z}^{(\lambda,\mathrm{Bi})}$ or its integrals are computed for a given λ or domain, and different approaches will be appropriate for different domains and for λ of different magnitudes. For example, many of the eigenvalues will be zero, in which case the solution is constant and no computation is required. Moreover, the intended quantity is not the pointwise solution but the integral of the solution (Eq. (19)); this sometimes leads to selection of a method different from the one that would typically be used for the pointwise solution. As an example, separation of variables solutions (Sec. 3.1) have slow pointwise convergence when the domain has corners, but the convergence of the integral of the solution is largely unaffected. A more thorough discussion of methods and domains is presented in Sec. 3.

2.3. Computation of Rates

Computation of the multi-step effectiveness vector (or computed rate) is done in three steps:

1. given $B(T)$, obtain the diagonalization ($\boldsymbol{\lambda}$ and R)
2. invert R to obtain $\boldsymbol{\alpha} = R^{-1}\boldsymbol{Y}_\infty$
3. for each λ_k obtain the corresponding $\eta(\lambda_k,\mathrm{Bi})$

Each of these steps may either be done online (i.e., for each required temperature and Biot number) or pre-computed (i.e., stored in a lookup table and looked up as needed). By caching the correct values, effectiveness factors for a given temperature and set of free stream concentrations can be found by a simple matrix multiplication. Many quantities, like multi-step effectiveness vectors (MEVs), can be computed using tables of these values.

Recall ϵ is the catalyst particle voidage, ρ_g is the case density, assumed to be the same inside and outside the particle, ψ is the deactivation due to coking, and $Y_{i,\infty}$ is the free stream mass fraction of the i-th species. At each point in the catalyst the i-th chemical is produced at a rate (mass per unit time) of

$$\epsilon\rho_g\left(-\sum_j\psi k_{ij}Y_i+\sum_j\psi k_{ji}Y_j\right)$$

which, when integrated over the volume of the catalyst particle V_p, yields change in mass of the i-th species due to particle p, which we will denote M_i^p, by

$$\frac{M_i^p}{\epsilon\rho_g} = -\sum_j\psi k_{ij}\int_{\hat{\Omega}}Y_i\,\mathrm{d}V+\sum_j\psi k_{ji}\int_{\hat{\Omega}}Y_j\,\mathrm{d}V \tag{22a}$$

$$= -\sum_j\psi k_{ij}V_p\eta_i^pY_{i,\infty}+\sum_j\psi k_{ji}V_p\eta_j^pY_{j,\infty}, \tag{22b}$$

where

$$Y_{i,\infty}\eta_i^p = \frac{1}{V_p}\int_{\hat{\Omega}}Y_i\,\mathrm{d}V. \tag{23}$$

(Note the components of the MEV η_i^p are distinct from the single-stage effectiveness factors $\eta(\lambda_k,\mathrm{Bi})$.) Eq. (22a) is preferred to Eq. (22b) because it recovers the correct reaction rate in the absence of some or all product species; the effectiveness factor is undefined in these cases. Further, it should be emphasized that, while the single-stage effectiveness factors $\eta(\lambda_k,\mathrm{Bi})$ are bounded between zero and one, the multi-stage effectiveness factors η_i^p may exceed one, as intermediate species may be created within the particle and promptly consumed. Also observe

$$\frac{M_i^pL^2}{V_p\epsilon\rho_g\mathcal{D}_i} = \left(B\bar{Y}\right)_i, \tag{24}$$

so we have

$$\frac{\boldsymbol{M}^p}{V_p\epsilon\rho_g} = \frac{1}{L^2}DR\Lambda R^{-1}R\,H(\boldsymbol{\lambda},\mathrm{Bi})R^{-1}\boldsymbol{Y}_\infty$$
$$= \frac{1}{L^2}DR\Lambda H(\boldsymbol{\lambda},\mathrm{Bi})R^{-1}\boldsymbol{Y}_\infty \tag{25a}$$
$$= \underbrace{\left(\underbrace{\left(\frac{1}{L^2}DR\right)}_{F}\Lambda H(\boldsymbol{\lambda},\mathrm{Bi})\underbrace{R^{-1}}_{G}\right)}_{E}\boldsymbol{Y}_\infty, \tag{25b}$$

where $H(\boldsymbol{\lambda},\mathrm{Bi})$ is the matrix with effectiveness factors $\eta(\lambda_k,\mathrm{Bi})$ (Eq. (20)) on the diagonal, Λ is the matrix with λ_i on the diagonal, and D is the matrix with $\bar{\mathcal{D}}_i$ on the diagonal. Recall the matrix B depends on the penalty to reaction rate due to accumulation of coke ψ multiplicatively, i.e. $B = \psi B'$ where B' is the (constant) matrix obtained in the case $\psi = 1$. The eigenvalues λ_k then depend multiplicatively (i.e., $\lambda_k = \psi\lambda'_k$) on ψ, but the eigendecomposition does not. There are then two reasonable sets of lookup tables to create: one if the nominal reaction rates are constant throughout the simulation, and one if environmental factors (e.g., accumulation of coke) effect the nominal reaction rates. In the case of constant reaction rates, store a table $T \mapsto E$ and compute

$$\frac{\boldsymbol{M}^p}{V_p\epsilon\rho_g} = E\boldsymbol{Y}_\infty. \tag{26}$$

If nominal reaction rates are modified by a factor ψ, store a table $(\lambda,\mathrm{Bi}) \mapsto \eta(\lambda,\mathrm{Bi})$ and a table $T \mapsto (\lambda_1,\ldots,\lambda_N,F,G)$ to compute

$$\frac{\boldsymbol{M}^p}{V_p\epsilon\rho_g} = F\mathrm{Diag}_k\left(\lambda_k\eta(\lambda_k,\mathrm{Bi})\right)G\boldsymbol{Y}_\infty. \tag{27}$$

Because $\eta(\lambda_k,\mathrm{Bi}) = \eta(\psi\lambda'_k,\mathrm{Bi})$ depends nonlinearly on ψ, we must either store the factorization information (as described here) or store a two dimensional table $(T, y_{CK}) \mapsto E$ where y_{CK} is the mass fraction of coke on the particle.

An explicit algorithm by which the MEV may be approximated is as follows.

Pre-processing:

1. Choose temperatures $T^{(1)} < T^{(2)} < \cdots < T^{(I)}$ spanning the range that may appear in the simulation.
2. For each $T^{(i)}$ compute the corresponding matrix $B(T^{(i)})$ and, per Eq. (19),

$$\boldsymbol{Y}^{(i)} = R\,\mathrm{Diag}_k\left(V_p\,\eta(\lambda_k,\mathrm{Bi})\right)R^{-1}\boldsymbol{Y}_\infty \tag{28}$$

To compute reaction rates: Given a temperature T,

1. Find i such that $T^{(i)} \le T \le T^{(i+1)}$.
2. Compute $w = \dfrac{T - T^{(i+1)}}{T^{(i)} - T^{(i+1)}}$.
3. Approximate the MEV

$$\boldsymbol{\eta} \approx w\boldsymbol{Y}^{(i)} + (1-w)\boldsymbol{Y}^{(i+1)}. \tag{29}$$

Here we use a linear interpolation in temperature; more complex interpolations (e.g. [16]) may be used as well. Some irreversible reactions may result in complex eigenvalues, requiring a two-dimensional interpolation to obtain single stage effectiveness factors; a thorough investigation of this is left for future research.

In the remainder of this paper, after some brief notes about diagonalization of B, we will discuss methods for finding single-stage solutions as they relate to the present application (Sec. 3) and present a proof of concept for usage of these computations in a CFD–DEM simulation (Sec. 4). Further, the authors of this code make available a library to assist in implementing these methods into reactor-scale codes.[1]

3. The Single-Stage Problem

To complete the computation introduced in Sec. 2.1, single-stage effectiveness factors are required. Single-stage effectiveness factors are defined as

$$\eta = \frac{1}{V_p}\int_\Omega Z\,\mathrm{d}V, \tag{30}$$

where Z solves

$$-\nabla^2 Z + a^2 Z = 0 \qquad \text{in } \Omega \tag{31a}$$
$$\mathrm{Bi}^{-1}\nabla Z\cdot\mathbf{n} + Z = 1 \qquad \text{on } \partial\Omega \tag{31b}$$

where $\mathbf{n}$ is the outward normal and Ω is the (dimensional or nondimensional) domain in question. For reversible reactions it is possible for eigenvalues of B to be complex; while that case is allowed in the diagonalizatio process, we will not discuss solutions to the single-stage problem in that case.

The topic of the single-stage effectiveness factor (for a^2 real) has been well-explored in the literature. However, we will briefly summarize some of the existing literature on this topic and comment upon the suitability of certain computation or estimation techniques for this particular purpose. The diagonalization process imposes no restrictions on the method that may be used for computation of single-stage effectiveness factors, presuming the eigenvalues of B remain real. The constraints that are important are numerical, both with regard to efficiency and minimization of error.

A general discussion effectiveness factors as well as simple expressions for spheres, slabs, and some other common shapes (Tbl. 2) can be found in standard texts (e.g. [18,

[1] Code written in Python for building pre-computed lookup tables can be found at github.com/johnpwakefield/mevlib.

Sphere	$\eta = \dfrac{3}{ar_p}\left(a\mathrm{Bi}^{-1} + \dfrac{ar_p\tanh(ar_p)}{ar_p - \tanh(ar_p)}\right)^{-1}$
Cylinder	$\eta = \lim_{N,K\to\infty}(A_N + B_K)$ $A_N = \sum_{n=0}^{N} \dfrac{16}{\pi^2 r_p p_n (2n+1)^2}\dfrac{I_1(p_n r_p)}{I_0(p_n r_p)}$ $B_K = \sum_{k=1}^{K} \dfrac{8}{h_p q_k j_k^2}\tanh\left(q_k\dfrac{h_p}{2}\right)$ $p_n = \sqrt{a^2 + \left(\dfrac{\pi(2n+1)}{h_p}\right)^2}$ $q_k = \sqrt{a^2 + \dfrac{j_k^2}{r_p^2}}$ j_k is the increasing sequence of zeros of J_0
Rectangular Prism	$\eta = \sum_{d\in\{x,y,z\}}\sum_{m,n} \dfrac{32}{\beta_{d,m,n}\pi^4\ell_{p,d}}\dfrac{1}{(2m+1)^2(2n+1)^2}\tanh\left(\beta_{d,m,n}\dfrac{\ell_{p,d}}{2}\right)$ $\beta_{d,m,n}^2 = a^2 + \sum_{d'\neq d}\left(\dfrac{\pi(2m+1)}{\ell_{p,d'}}\right)^2$
General Geometries (Aris [17])	$\eta = \dfrac{1}{\Phi}\left(\coth 3\Phi - \dfrac{1}{3\Phi}\right)$ $\Phi^2 = \left(\dfrac{V_p}{S_p}\right)^2 \dfrac{k}{D_{\mathrm{eff}}}$

Table 2: Single-stage effectiveness factors η for a variety of shapes.

19, 15, 13]). Effectiveness factors for shapes like cylinders [8] or prisms can be found exactly through separation of variables; these are discussed further in Sec. 3.1.

Some estimation techniques for general shapes also exist [17, 18, 20]. In particular, the approximation for spherical geometry with the proper nondimensionalization is often used regardless of geometry, with minimal error [21, 22]. However, the propogation of these errors through the diagonalization process for coupled reactions has yet to be studied. Further discussion of general estimates for effectiveness factors can be found in [21, 22, 23, 17, 19, 15, 18].

For the present application, fast and accurate evaluations of effectiveness factors are required. Evaluation of an exact (potentially unclosed) form (e.g. from Sec. 3.1) may be extremely slow in practice. More general estimates may prove to be useful here, but further study of the propogation of the error in these estimates through the diagonalization process is required. For the proof of concept that follows, simple lookup tables with interpolation are used. Interpolation error is well understood, the time required to interpolate from a one dimensional table is negligible, and the required computation time to obtain single stage effectiveness factors is not incurred at runtime; the time required to compile a table ahead of time is negligible.

3.1. Separation of Variables

Separation of variables, sometimes referred to as expansion in eigenfunctions, is a well-known technique by which many linear PDEs in some domains may be solved. A thorough treatment of this simple technique may be found in any standard PDE text, e.g. [24]. We will, however, comment on the suitability of these solutions for the purpose of providing single-stage effectiveness factors in the present context, using the cylinder as an illustrative example. The separation of variables solution for Eq. (31) relies on well-known properties of Bessel functions [25, 26], was first presented in the context of chemical engineering

by Gunn [8], and has been commented on by later authors [9]. This approach is difficult to modify for finite Biot number, so we have taken $\mathrm{Bi}^{-1} = 0$ for this discussion.

The solution in the interior of the cylinder is given by

$$Z(r,z) = Z_1(r,z) + Z_2(r,z) \tag{32}$$

where

$$Z_1(r,z) = \sum_{n=0}^{\infty} \frac{4}{\pi(2n+1)} \sin\left(\frac{\pi(2n+1)}{h_p} z\right) \frac{I_0\left(\upsilon_n r\right)}{I_0\left(\upsilon_n r_p\right)} \tag{33}$$

with

$$\upsilon_n^2 = a^2 + \frac{\pi^2}{h_p^2}(2n+1)^2$$

and

$$Z_2(r,z) = 2\sum_{k=1}^{\infty} \frac{\cosh\left(\sqrt{a^2 + \frac{j_k^2}{r_p^2}}\left(z - \frac{h_p}{2}\right)\right)}{\cosh\left(\sqrt{a^2 + \frac{j_k^2}{r_p^2}}\,\frac{h_p}{2}\right)} \frac{J_0\left(\frac{j_k}{r_p} r\right)}{j_k J_1(j_k)}, \tag{34}$$

where j_k are the increasing sequence of zeros of J_1. The corresponding effectiveness factor is presented in Tbl. 2.

For the present application the single stage effectiveness factor must be evaluated once for every active species for every temperature present in the domain. The required frequency of evaluation makes non-closed forms like those obtained from separation of variables considerably expensive. One approach to this problem is to determine an exact or heuristic number of terms that must be evaluated to obtain the desired error. For example, the formula for the effectiveness factor in a cylinder (Tbl. 2) has two distinct parts, whose relative importance is highly dependent upon the aspect ratio γ (see Fig. 1). To utilize these estimates without precompilation of tables, functions $K(\delta,\gamma)$ and $N(\delta,\gamma)$ such that

$$|A_{N(\delta,\gamma)} - A_\infty + B_{K(\delta,\gamma)} - B_\infty| < \delta \tag{35}$$

and

$$\iota_A N(\delta,\gamma) + \iota_B K(\delta,\gamma), \tag{36}$$

where ι_A and ι_B are the computational costs of computing a single term in A_N and B_K respectively would need to be found. This is essentially the problem addressed in [23, 9]. Another technique not explored in the literature is to utilize series convergence acceleration techniques (e.g. Aitken acceleration, see [27] for an overview) in the context of these series. Figure 2 shows convergence of sums A_N and B_K (see Tbl. 2) as a function of computational 'cost units.' One 'cost unit' is approximately the the time it takes to perform one floating point multiplication; this accurately weights the high cost of evaluating Bessel functions. Ultimately, the computational time taken to estimate the single-stage effectiveness factor is unacceptable for a computation that must be performed separately for hundreds of thousands of particles in a complex simulation, but negligible in the context of a single computation or pre-computation of a table.

4. Integration into Reactor Models

We will now turn our attention to an CFD–DEM simulation of an FCC unit using the kinetics from Xiong et al. [28]. For the present mechanism with particles of diameter $d_p = 210\,\mu\mathrm{m}$ the leading eigenvalue (with nondimensionalization by the particle diameter) of $\lambda_1 = b_{11} \approx 9.6331$ corresponds to a single-stage effectiveness factor of $\eta(\lambda_1, 0) \approx 0.6591$; reaction rates computed with diffusion limitations differ significantly from those computed without in this case. Following Lattanzi et al. [12] we use the correlation of Sirkar [29] and obtain Biot numbers on the order of 500 to 8000, depending on the species weight, justifying the use of the $\mathrm{Bi} \to \infty$ limiting case. Simulations are performed within NGA, a second-order, finite volume, variable density, low Mach number code [30, 31, 4]. A semi implicit Crank–Nicholson scheme was used to achieve second order accuracy in time. The bounded quadratic upwind biased interpolative convective scheme (BQUICK) [32] was used for advancement of scalars (e.g., mass fractions). In this section we will describe how heterogeneous chemistry with rates computed per Sec. 2.1 may be integrated into such a code. This both provides a proof of concept for the present approach (and by extension [12]) as well as an guide for future implementations of similar rate computations.

Though the catalyst particle contains a mixture of solid catalyst and gas, in the description that follows we will treat the region containing the catalyst particle as solid; we are operating under the assumption that the pores are small enough that flow through them is negligible compared to the fluid outside the catalyst. For chemistry, it is assumed the concentration gradient inside the catalyst particle does not deviate significantly from the steady state solution at any given time, i.e. any change of the boundary condition results in a near instantaneous adaptation of the interior to the corresponding steady state solution. This avoids the need for a mass balance between the catalyst pores and the surrounding fluid (e.g., see [7, 33]). For this reason, the amount of any particular gas-phase reactant inside the catalyst particle is determined by the surrounding flow and the steady-state solution, and only the reaction rate is required. For other models of this type see [3, 34, 5].

4.1. Governing Equations

In the gaseous phase (outside the superficial particle volume) conservation of mass for each species is given by

$$\frac{\partial}{\partial t}\left(\varepsilon_g \rho_g Y_{g,i}\right) + \nabla\cdot\left(\varepsilon_g \rho_g Y_{g,i} \boldsymbol{u}_g\right) = \varepsilon_g \nabla\cdot\left(\rho_g \mathcal{D}_{g,i} \nabla Y_{g,i}\right) + \mathcal{M}_i, \tag{37}$$

where ρ_g is the gas density, ε_g is the gas volume fraction, $Y_{g,i}$ is the mass fraction in the gaseous phase of the

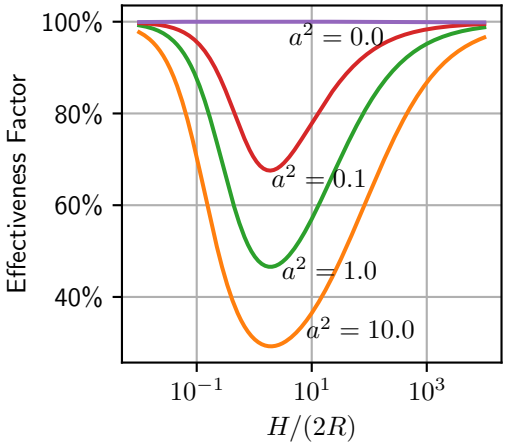

(a) Effectiveness factor η as a function of Thiele modulus a^2 (equivalent to eigenvalues in the multi-step case) and aspect ratio.

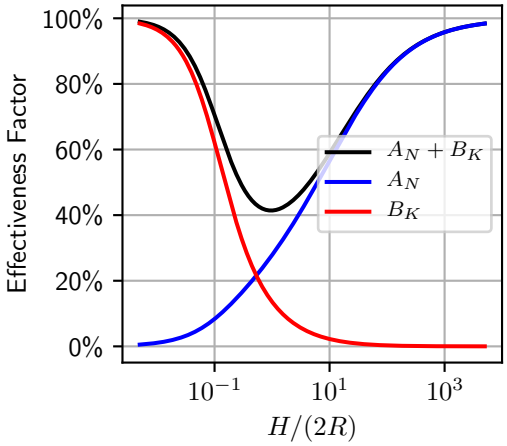

(b) Effectiveness factor and constituent parts A_N and B_K (see Tbl. 2) as a function of aspect ratio.

Figure 1: Effectiveness factor in a cylinder as a function of aspect ratio.

Table 3: Species and Catalyst Parameters

(a) Molecular weights of lump species.

Species	Mol. Weight $[\mathrm{g \cdot mol^{-1}}]$
Feed Oil (S)	444.0
Diesel (D)	230.0
Gasoline (G)	115.0
Liquid Petroleum Gas (LPG)	52.0
Dry Gas (D_R)	16.0
Coke (C_K)	400.0

(b) Particle parameters need to compute diffusion coefficients per Eq. (5).

Pore Diameter (D_{pore})	0.002
Voidage (ϵ)	0.319
Tortuosity (τ)	7.0

i-th species, $\boldsymbol{u}_g$ is the gas phase velocity, $\mathcal{D}_{g,i}$ is the gas phase diffusivity of the i-th species, and $\mathcal{M}_i$ is the chemical source term for the i-th species (see Table 5). Details on the formulation of Eq. (37) can be found in [31]. Because we are operating in the CFD–DEM framework, $\mathcal{M}_i$ is ultimately obtained from projecting the source terms for each particle M_i^p (Eqs. (22), (26), (27)). These equations can be summed to obtain total mass conservation

$$\frac{\partial}{\partial t}\left(\varepsilon_g \rho_g\right) + \nabla \cdot \left(\varepsilon_g \rho_g \boldsymbol{u}_g\right) = \sum_j \mathcal{M}_j. \tag{38}$$

In the absence of mass transfer from the gas phase to the solid phase the right-hand side of Eq. (38) is zero. If coke is generated, then

$$\sum_j \mathcal{M}_j = -\mathcal{M}_{\mathrm{CK}}. \tag{39}$$

Similarly, conservation of momentum is given by

$$\frac{\partial}{\partial t}\left(\varepsilon_g \rho_g \boldsymbol{u}_g\right) + \nabla \cdot \left(\varepsilon_g \rho_g \boldsymbol{u}_g \boldsymbol{u}_g\right) = \varepsilon_g \nabla \cdot \boldsymbol{\tau}_g + \boldsymbol{\mathcal{F}} + \varepsilon_g \rho_g \boldsymbol{g}, \tag{40}$$

where

$$\boldsymbol{\tau}_g = -p_g \boldsymbol{I} + \mu_g \left(\nabla \boldsymbol{u}_g + \left(\nabla \boldsymbol{u}_g\right)^T - \frac{2}{3}\left(\nabla \cdot \boldsymbol{u}_g\right) \boldsymbol{I} \right) \tag{41}$$

is the stress tensor, p_g is the pressure, μ_g is the dynamic viscosity, $\boldsymbol{I}$ is the identity tensor, $\boldsymbol{\mathcal{F}}$ are forces between the particles and the fluid, and $\boldsymbol{g}$ is acceleration due to gravity. Viscosity μ_g is held constant (Table 5). We employ the equation of state for an ideal gas

$$P_g = \frac{\rho_g}{W} \mathcal{R} T_g, \tag{42}$$

where P_g is the static pressure, W is the mixture molecular weight ($W^{-1} = \sum_j Y_j / W_j$) and $\mathcal{R}$ is the ideal gas constant. The molecular weights used for the demonstrations in this section can be found in Table 3a.

Mass source terms are given by Eqs. (22a) and (22b). The free stream mass fractions are given by the mass fractions in the fluid phase interpolated at the particle location $\boldsymbol{Y}_\infty = \boldsymbol{Y}|_{\boldsymbol{x}_p}$. For species other than coke, mass exchange is projected onto the Eulerian mesh (Eq. (47)). For coke, this remains the correct formula for generated mass, but this mass stays on the particle, making the mass of the particle the sum of the catalyst mass and the mass of the coke

$$m_p = m_p^{\mathrm{CA}} + m_p^{\mathrm{CK}}. \tag{43}$$

The mass of the catalyst m_p^{CA} is constant, but the mass of

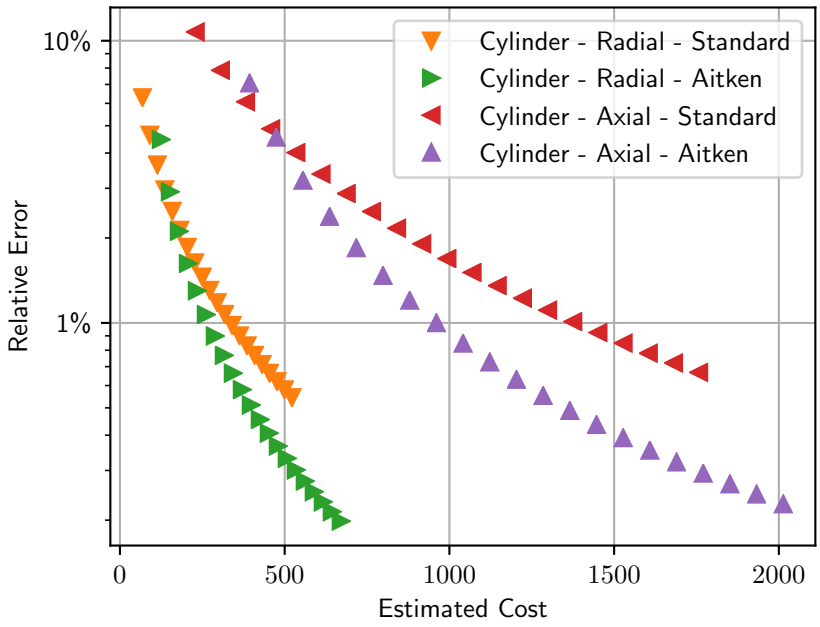

Figure 2: Convergence of the single-stage effectiveness factor in a cylinder.

coke changes per

$$\frac{\mathrm{d}m_p^{\mathrm{CK}}}{\mathrm{d}t} = M_{\mathrm{CK}}^p. \tag{44}$$

The motion of the p-th particle is governed by

$$\begin{aligned} \frac{\mathrm{d}\boldsymbol{x}_p}{\mathrm{d}t} &= \boldsymbol{u}_p \\ m_p \frac{\mathrm{d}\boldsymbol{u}_p}{\mathrm{d}t} &= V_p \nabla \cdot \tau_g|_{\boldsymbol{x}_p} + \boldsymbol{f}_p^{\mathrm{drag}} + \frac{\mathrm{d}m_p}{\mathrm{d}t}\boldsymbol{u}_p + m_p \boldsymbol{g} + \boldsymbol{C} \end{aligned} \tag{45}$$

where

$$\boldsymbol{f}_p^{\mathrm{drag}} = m_p \frac{\epsilon_g}{\tau_p} \left(\boldsymbol{u}_{g@p} - \boldsymbol{u}_p\right) F(\epsilon_g, \mathrm{Re}_p), \tag{46}$$

and $\boldsymbol{C}$ is the force of collisions. In the expression above, $\mathrm{Re}_p = \epsilon_g \rho_g \left|\boldsymbol{u}_{g@p} - \boldsymbol{u}_p\right| d_p/\mu_g$, where d_p is the particle diameter and $\boldsymbol{u}_{g@p}$ is the gas velocity evaluated at the particle position. For the proof of concept presented here, the particles are treated as spheres to make use of standard models for drag and collisions. For non-spherical particles, development of accurate approximations to drag remain an active area of research [35, 36, 37]. Here, the drag correlation of Tenneti et al. [38], valid for spheres at finite volume fraction and Reynolds number, is used. The force of collisions $\boldsymbol{C}$ are modeled by the soft-sphere model of Cundall and Strack [39] with coefficient of restitution $\mathrm{e} = 0.8$. At present, heat transfer between the phases is ignored and the temperature is held constant at 600 °C. Because this is a proof of concept for the general method presented above, the interpolation from a table of relevant temperatures is conducted nonetheless.

Information from particle p to the fluid mesh, namely the rate of mass accumulation/destruction of species i, M_i^p, and the force, are projected onto the fluid mesh by

$$\mathcal{M}_i(\boldsymbol{x}) = \sum_{p=1}^{N_p} \mathcal{G}\left(|\boldsymbol{x} - \boldsymbol{x}_p|\right) M_i^p \tag{47}$$

and

$$\boldsymbol{\mathcal{F}}(\boldsymbol{x}) = \sum_{p=1}^{N_p} \mathcal{G}\left(|\boldsymbol{x} - \boldsymbol{x}_p|\right) \left(\boldsymbol{f}_p^{\mathrm{drag}} + \frac{\mathrm{d}m_p}{\mathrm{d}t}\boldsymbol{u}_p\right), \tag{48}$$

respectively, where $\mathcal{G}$ is the smoothing Kernel taken to be Gaussian with a characteristic size of $7d_p$. Further details can be found in Capecelatro and Desjardins [31]. To summarize, single stage effectiveness factors (Sec. 3) are used in Eq. (25b) to compute effective reaction rates (Eq. (21)) by

$$\begin{aligned} \boldsymbol{M}^p &= E\boldsymbol{Y}_\infty && \text{(49a)} \\ &= F\mathrm{Diag}_k\left(\lambda_k \eta(\lambda_k, \mathrm{Bi})\right) G\boldsymbol{Y}_\infty, && \text{(49b)} \end{aligned}$$

where the former (Eq. (49a)) is used when deactivation due to coking is not modeled and the latter (Eq. (49b)) is used when it is. These are then, for CFD–DEM, projected onto the computational mesh via Eq. (47).

4.2. Reaction Mechanism

Figure 3 depicts the reaction mechanism considered in the present study proposed by [28] and used in [12]. Reaction parameters are shown in Tables 3 and 4. Each reaction

Table 4: Reaction coefficients (see Fig. 3). All reactions are at reference temperature 773K.

Reaction	Pre-Exponential Factor (A_{ij}) [s^{-1}]	Activation Energy (Ea_{ij}) [$kJ \cdot mol^{-1}$]
$S \to D$ (k_{12})	1.413	47.6
$S \to G$ (k_{13})	4.337	43.4
$S \to LPG$ (k_{14})	1.163	38.5
$S \to D_R$ (k_{15})	0.114	30.2
$S \to C_K$ (k_{16})	0.386	30.0
$D \to G$ (k_{23})	0.229	54.1
$D \to LPG$ (k_{24})	0.161	62.9
$D \to D_R$ (k_{25})	0.041	66.7
$D \to C_K$ (k_{26})	0.137	65.0
$G \to LPG$ (k_{34})	0.128	80.5
$G \to D_R$ (k_{35})	0.030	85.2
$G \to C_K$ (k_{36})	0.103	77.3

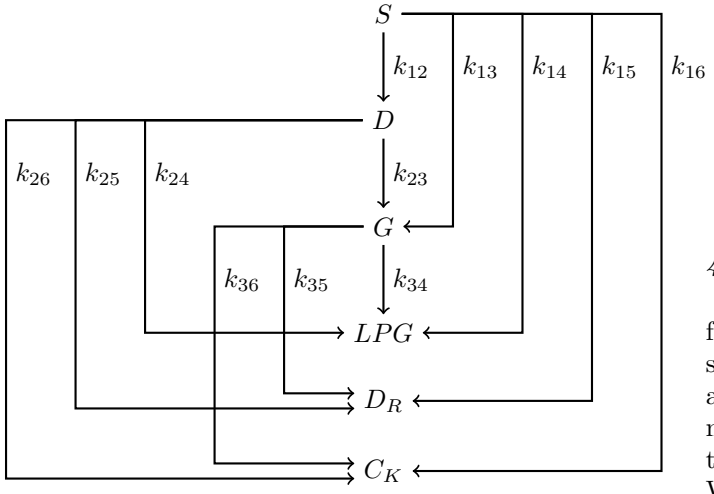

Figure 3: A schematic of the reaction mechanism originally from [28] and used in [12].

rate constant is of the form

$$k_{ij} = A_{ij} \exp\left(-\frac{\mathrm{Ea}_{ij}}{\mathcal{R}}\left(\frac{1}{T_g} - \frac{1}{T_0}\right)\right), \tag{50}$$

where A_{ij} is a pre-exponential factor, Ea_{ij} is the activation energy, $\mathcal{R}$ is the ideal gas constant, and $T_0 = 773\,\mathrm{K}$ is the reference temperature. For reactions that do not take place, $A_{ij} = 0$. The matrix K becomes

$$\Xi = \begin{array}{c} \begin{matrix} S & D & G & LPG & D_R & D_K \end{matrix} \\ \begin{bmatrix} 0 & k_{12} & k_{13} & k_{14} & k_{15} & k_{16} \\ 0 & 0 & k_{23} & k_{24} & k_{25} & k_{26} \\ 0 & 0 & 0 & k_{34} & k_{35} & k_{36} \\ 0 & 0 & 0 & 0 & 0 & 0 \\ 0 & 0 & 0 & 0 & 0 & 0 \\ 0 & 0 & 0 & 0 & 0 & 0 \end{bmatrix} \end{array} \begin{matrix} S \\ D \\ G \\ LPG \\ D_R \\ C_K \end{matrix}.$$

4.3. Particle in a Box

Before proceeding to CFD–DEM, we demonstrate the framework on an ODE model. Consider a case in which a single catalyst particle of diameter 400 µm is placed inside a small, periodic domain with feed oil (S). Here 'small' means that the time required for the concentration outside the superficial particle to become uniform is negligible. We would in this case expect over time to be left with liquid petroleum gas (LPG), dry gas (D_R), and coke (C_K). If we further assume that the gas phase is fully mixed, i.e. the mass fractions of each of the preceding species is constant in the gas phase, then this becomes a simple ODE that we can use to illustrate the chemistry model described above without the complications of fluid flow around the particles. This is in essence a zero dimensional model; the reaction rates discussed here may be used for these models as well.

The domain, denoted by V, is an L^3 box with initial mass fractions

$$(Y_\infty^S, Y_\infty^D, Y_\infty^G, Y_\infty^{LPG}, Y_\infty^{D_R}) = (0.80, 0.00, 0.00, 0.00, 0.00).$$

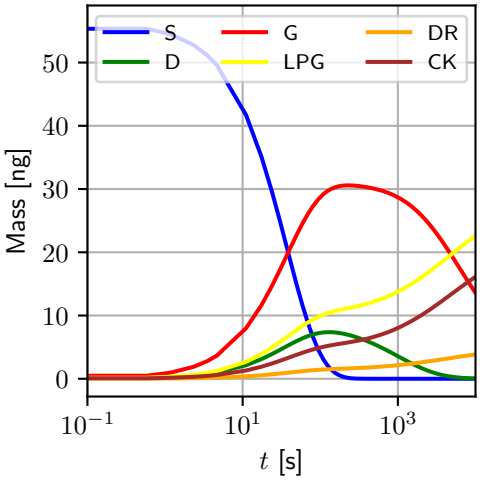

Figure 4: Species mass as a function of time computed with catalyst deactivation from accumulation of coke as approximated by the ODE model (Eq. (52)).

Under the perfect mixing assumption, the mean gaseous mass fraction in the domain is the same as the mass fraction at the boundary of the particle, so

$$L^3 Y_{i,\infty} = \int_V Y_{g,i} \, \mathrm{d}V. \tag{51}$$

Using Eqs. (22) we can then write an ODE for the (homogeneous) gaseous volume fractions inside this box as

$$\frac{\mathrm{d}}{\mathrm{d}t} \varepsilon_g \rho_g Y_{i,\infty} = \frac{\mathrm{d}}{\mathrm{d}t} \int_V \varepsilon_g \rho_g Y_{g,i} \, \mathrm{d}V = \int_V \mathcal{M}_i \, \mathrm{d}V = M_i^p. \tag{52}$$

Eq. (26) or (27) can be used to evaluate the right-hand side. Note that, because coke is produced and remains on the particle, the gas density ρ_g is a dynamic quantity. Results of the resulting simulation with catalyst deactivation due to coking is shown in Fig. 4. As expected, the three reacting species S, G, and DR are consumed over time, leaving a distribution of D, LPG, and CK over long enough timescales. Because the total amount of reactants are limited, the influence of coke accumulation in this scenario are small.

4.4. Fluidized Bed

We will now turn our attention to a two-dimensional CFD–DEM simulation of a fluidized bed reactor. The simulations are based on the cases in [40], but with catalyst properties and kinetics to match [12, 28]. The fluidized bed has a width of 0.15 m and a height of 0.3 m; it is approximated by a 384×768 mesh. The domain contains 212552 spherical particles with a diameter of 210 µm, material density of $1160\,\mathrm{kg \cdot m^{-3}}$, and internal voidage of $\epsilon \approx 0.319$ (see Tbl. 5). Particles are held in a plane, but a domain thickness of 300 µm was used for volume fraction computations [41]. The inflow velocity was chosen to be $0.1434\,\mathrm{m \cdot s^{-1}}$, in the range of 7-12 times the minimum fluidization velocity. The inflow gas contains only feed oil, with component mass fractions

$$(Y_S^{\mathrm{in}}, Y_D^{\mathrm{in}}, Y_G^{\mathrm{in}}, Y_{LPG}^{\mathrm{in}}, Y_{DR}^{\mathrm{in}}) = (0.04, 0.00, 0.00, 0.00, 0.00).$$

Coke (CK) does accumulate on the particles and the mass of the particles does change as a result, but the accumulation is not significant over the timescales considered.

Table 5: Parameters for the fluidized bed test case.

Domain Dimensions	$30\,\mathrm{mm} \times 15\,\mathrm{mm}$
Eulerian Mesh	768×384
Particle Diameter	210 µm
Number of Particles	212552
Inlet Velocity	$0.1434\,\mathrm{m \cdot s^{-1}}$
Particle Voidage (ϵ)	0.319
Particle Material Density	$1160\,\mathrm{kg \cdot m^{-3}}$
Force of Gravity (g)	$9.81\,\mathrm{m \cdot s^{-2}}$
Temperature	600 K
Dynamic Viscosity (μ_g)	$3.1462 \times 10^{-5}\,\mathrm{N \cdot s \cdot m^{-2}}$
Species Diffusivity ($\mathcal{D}_{g,i}$)	$4.4946 \times 10^{-5}\,\mathrm{m^2 \cdot s^{-1}}$

Figure 5 depicts a fully evolved state ($t = 5.4\,\mathrm{s}$). First, significant differences in mass conversion exist at different points across the width of the bed, and these effects can be seen in the flow downstream of the top of the bed. This strongly suggests that the bubbling structure of the bed influences reaction rates in a manner not captured by models compartmentalized in only the vertical direction. Quantitative agreement of models with experimental fluidized bed reactors will require not only accurate reaction rates in the vicinity of individual particles, but also modeling of the fluidized bed within which those particles exist. It is likely that, even in the absence of quantitative accuracy, models of this type can be qualitatively useful in the design of efficient fluidized bed reactors.

The breakdown of average time spent in each routine during a single timestep of the CFD–DEM simulation is given in Fig. 6. The majority of the time is spent solving the pressure Poisson equation to enforce continuity (Eq. (38)). We briefly note that the pressure Poisson equation was solved via an efficient multigrid method, and other solution procedures are unlikely to result in significantly reduced time. The particle update (Eq. (45)) contributes to approximately 30% of the time, with the majority spent in computing collisions. Here, collisions are solved using nearest-neighbor detection that scales as $\mathcal{O}(N_p \log N_p)$ where N_p the number of particles. Most importantly, the computation of reaction rates only contributes to $\sim 2\%$ of the total time due to the use of efficient lookup tables. Thus, the proposed framework allows for intraparticle dynamics to be captured in a reactor-scale model at negligible cost.

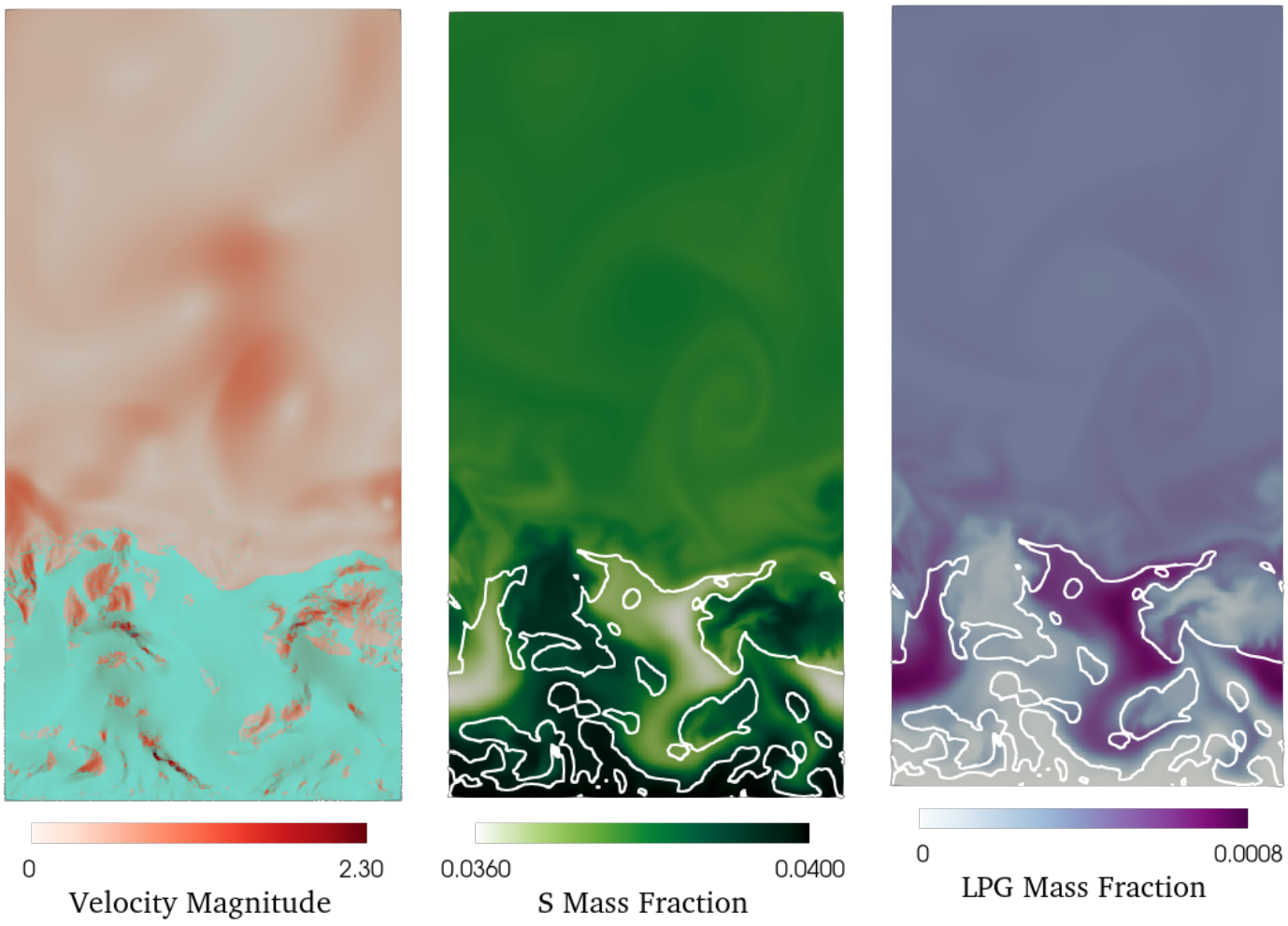

(a) Particle positions (teal) and magnitude of fluid velocity (red/white).

(b) Feed Oil (S) concentration (white/green) with white contours at $\epsilon_f = 0.7$.

(c) Liquefied Petroleum Gas (LPG) concentration (purple/white) with white contours at $\epsilon_f = 0.7$.

Figure 5: A fully evolved state of the fluidized bed test case.

5. Conclusions and Areas for Future Research

This work presents a general framework for modeling of first order heterogeneous chemical reactions in porous particles. Open source code is provided that generates pre-computed lookup tables for efficient implementation in CFD–DEM. The proposed methodology is built under the assumptions that the interior can be described with constant diffusion coefficients, the Biot number describing the boundary condition does not vary significantly between species, and the intraparticle dynamics maintain a quasi-steady state. The constraints on chemistry are clearly separate from constraints on geometry, and a computationally efficient scheme for approximating rates in CFD simulations is obtained by decomposing the problem into decoupled subproblems. Single stage effectiveness factors for a variety of common catalyst shapes are summarized (Tbl. 2). The available code and estimates should accelerate the introduction of this functionality into other CFD codes by providing pre-processing steps.

The limitations of this approach lead directly to avenues for future work. The ostensible goal of the present work is to assist in design of particle and reactor geometry taking into account the dynamics of the reactor (i.e., models including particles moving within a fluid rather than a one dimensional model of a bed of particles). At the desired scale, resolving the interior of the particle is impractical, but there may be better simplified models for reaction rates within a single particle.

Efficient methods for solving single-stage problems in the presence of small Biot numbers also remain an area for future research. Reversible reactions may introduce complex eigenvalues and, while the diagonalization is still valid, the single-stage problem becomes complex, requiring different numerical or analytical methods for computing integrals of solutions. Further, should interpolation be used in this case, the validity of a two dimensional interpolation in this context would need to be explored.

The model for coking (or other environmental penalties

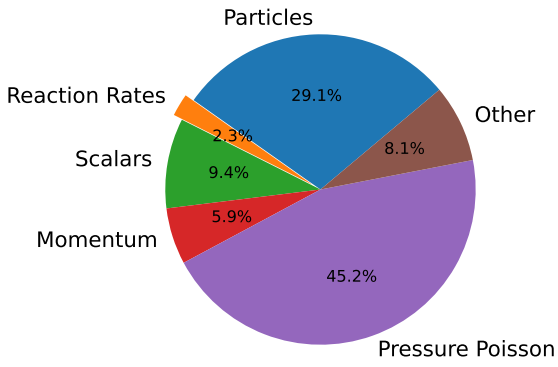

Figure 6: Distribution of time spent computing a single timestep of the CFD–DEM simulations with the parameters in Table 5. The subject of the present work falls within the 'Reaction Rates' category. 'Particles' consists of drag computations, projection of quantities to and from the mesh, and resolving particle collisions.

expressed through ψ) are assumed to be uniform throughout the particle. Exact or approximate site tracking remains an area for future research. Practical models for inhomogeneous deactivation within catalyst particles in the context of simulations of many particles will require reduced order representations of historical reaction sites, and it is at this point unclear what a practical representation of these distributions would be.

The restrictions on types of chemical reactions are significant; the requirement of first order kinetics is particularly restrictive. For the diagonalization proposed in [12] to be possible, Eq. (2) must be linear in mass fraction (or equivalently, concentration). A violation of this assumption would either require discovery of an equivalent tensor decomposition for polynomial dependence (e.g. second order reactions) upon mass fraction or a clever nonlinear decoupling technique in the general case.

The boundary conditions for reacting particles remains an important area of research more generally. The exterior of the catalyst particle is clearly more available than the porous interior; it is possible the integral of the bulk near the superficial boundary of the particle is not the appropriate estimate. Mass transport at the superficial boundary of the reacting particle is affected by the aforementioned geometry problems, the fluid boundary layer, the difference in (effective) diffusion at the boundary, the frequent proximity of other catalyst particles in the intended application, and the precise location at which the 'free stream' boundary values are estimated. There is not at present sufficient models for the interplay of these effects.

This generalized approach for quickly computing multi-stage reaction rates provides a framework for applications to other catalysis and pyrolysis processes (e.g. [42]), adsorption of CO_2 [43, 2] or SO_2 [44], among others. Applying this method to another application only requires computing the matrix B from reaction rates, determining the regimes of the eigenvalues of this matrix, and solving the single-stage problem for these eigenvalues. Though the single-stage problem may prove difficult in some of those cases (e.g. in the case of complex eigenvalues), standard methods for approaching these problems exist, and the computation of those solutions can be separated from the online computational cost. For the case of real eigenvalues (e.g. in the case of irreversible reactions), general estimates have been presented that are independent of geometry, providing an alternative to a second interpolation. Computationally feasible corrections of reaction rates due to intraparticle diffusion limitations both in catalysis and other applications has the potential to improve accuracy of small-scale and reactor-scale simulations across concentration, temperature, and particle size/shape regimes.

Acknowledgments

This project is was funded by the National Renewable Energy Laboratory (NREL) under US Department of Energy contract number SUB-2021-10408.

References

[1] V. Chandra, E. Peters, J. Kuipers, Direct numerical simulation of a non-isothermal non-adiabatic packed bed reactor, Chemical Engineering Journal 385 (2020) 123641. doi:10.1016/j.cej.2019.123641.

[2] R. T. Driessen, J. J. van der Linden, S. R. Kersten, M. J. Bos, D. W. Brilman, Characterization of mass transfer in a shallow fluidized bed for adsorption processes: Modeling and supporting experiments, Chemical Engineering Journal 388 (2020) 123931. doi:10.1016/j.cej.2019.123931.

[3] D. Micale, R. Uglietti, M. Bracconi, M. Maestri, Coupling Euler–Euler and Microkinetic Modeling for the Simulation of Fluidized Bed Reactors: an Application to the Oxidative Coupling of Methane, Industrial & Engineering Chemistry Research 60 (2021) 6687–6697. doi:10.1021/acs.iecr.0c05845.

[4] S. Beetham, J. Capecelatro, Biomass pyrolysis in fully-developed turbulent riser flow, Renewable Energy 140 (2019) 751–760. doi:10.1016/j.renene.2019.03.095.

[5] C. Wu, Y. Cheng, Y. Ding, Y. Jin, CFD–DEM simulation of gas–solid reacting flows in fluid catalytic cracking (FCC) process, Chemical Engineering Science 65 (2010) 542–549. doi:10.1016/j.ces.2009.06.026.

[6] H. Goyal, O. Desjardins, P. Pepiot, J. Capecelatro, A computational study of the effects of multiphase dynamics in catalytic upgrading of biomass pyrolysis vapor, AIChE Journal 64 (2018) 3341–3353. doi:10.1002/aic.16184.

[7] R. Uglietti, M. Bracconi, M. Maestri, Coupling CFD–DEM and microkinetic modeling of surface chemistry for the simulation of catalytic fluidized systems, Reaction Chemistry & Engineering 3 (2018) 527–539. doi:10.1039/C8RE00050F.

[8] D. Gunn, Diffusion and chemical reaction in catalysis and absorption, Chemical Engineering Science 22 (1967) 1439–1455. doi:10.1016/0009-2509(67)80071-X.

[9] M. Asif, Efficient Expressions for Effectiveness Factor for a Finite Cylinder, Chemical Engineering Research and Design 82 (2004) 605–610. doi:10.1205/026387604323142658.

[10] J. Zhu, S. S. Araya, X. Cui, S. K. Kær, The role of effectiveness factor on the modeling of methanol steam reforming over CuO/ZnO/Al2O3 catalyst in a multi-tubular reactor, International Journal of Hydrogen Energy 47 (2022) 8700–8715. doi:10.1016/j.ijhydene.2021.12.223.

[11] J. Wei, Intraparticle diffusion effects in complex systems of first order reactions I. The effects in single particles, Journal of Catalysis 1 (1962) 526–537. doi:10.1016/0021-9517(62)90125-2.

[12] A. M. Lattanzi, M. B. Pecha, V. S. Bharadwaj, P. N. Ciesielski, Beyond the effectiveness factor: Multi-step reactions with intraparticle diffusion limitations, Chemical Engineering Journal 380 (2020) 122507. doi:10.1016/j.cej.2019.122507.

[13] R. E. Cunningham, R. J. J. Williams, Diffusion in Gases and Porous Media, Springer US, Boston, MA, 1980. doi:10.1007/978-1-4757-4983-0.

[14] W. Kast, C.-R. Hohenthanner, Mass transfer within the gas-phase of porous media, International Journal of Heat and Mass Transfer 43 (2000) 807–823. doi:10.1016/S0017-9310(99)00158-1.

[15] R. B. Bird, W. E. Stewart, E. N. Lightfoot, Transport Phenomena, J. Wiley, 2002. Google-Books-ID: wYnRQwAACAAJ.

[16] M. Bode, N. Collier, F. Bisetti, H. Pitsch, Adaptive chemistry lookup tables for combustion simulations using optimal B-spline interpolants, Combustion Theory and Modelling 23 (2019) 674–699. doi:10.1080/13647830.2019.1583379.

[17] R. Aris, On Shape Factors for Irregular Particles–I. The Steady-State Problem. Diffusion and Reaction, Chemical Engineering Sciences 6 (1957) 262–268.

[18] R. Aris, The Mathematical Theory of Diffusion and Reaction in Permeable Catalysts: The theory of the steady state, Clarendon Press, 1975. Google-Books-ID: aT1RAAAAMAAJ.

[19] R. J. Wijngaarden, A. Kronberg, K. R. Westerterp, Industrial Catalysis: Optimizing Catalysts and Processes, WILEY-VCH, 1998. Google-Books-ID: YCJJ4VSQ1_cC.

[20] K. B. Bischoff, Effectiveness factors for general reaction rate forms, AIChE Journal 11 (1965) 351–355. doi:10.1002/aic.690110229.

[21] H. Shariff, M. H. Al-Dahhan, Analyzing the impact of implementing different approaches of the approximation of the catalyst effectiveness factor on the prediction of the performance of trickle bed reactors, Catalysis Today 353 (2020) 134–145. doi:10.1016/j.cattod.2019.07.033.

[22] P. Jeyabarathi, L. Rajendran, M. Abukhaled, M. Kannan, Semi-analytical expressions for the concentrations and effectiveness factor for the three general catalyst shapes, Reaction Kinetics, Mechanisms and Catalysis 135 (2022) 1739–1754. doi:10.1007/s11144-022-02205-x.

[23] A. Burghardt, A. Kubaczka, Generalization of the effectiveness factor for any shape of a catalyst pellet, Chemical Engineering and Processing: Process Intensification 35 (1996) 65–74. doi:10.1016/0255-2701(95)04115-X.

[24] L. C. Evans, Partial Differential Equations, volume 19 of *Graduate Studies in Mathematics*, second ed., American Mathematical Society, 2010.

[25] G. N. Watson, A Treatise on the Theory of Bessel Functions, 2nd ed., Cambridge University Press, 1922.

[26] DLMF, *NIST Digital Library of Mathematical Functions*, URL: http://dlmf.nist.gov/, f. W. J. Olver, A. B. Olde Daalhuis, D. W. Lozier, B. I. Schneider, R. F. Boisvert, C. W. Clark, B. R. Miller, B. V. Saunders, H. S. Cohl, and M. A. McClain, eds.

[27] N. Osada, Acceleration Methods for Slowly Convergent Sequences and their Applications, 1993.

[28] K. Xiong, C. Lu, Z. Wang, X. Gao, Kinetic study of catalytic cracking of heavy oil over an in-situ crystallized FCC catalyst, Fuel 142 (2015) 65–72. doi:10.1016/j.fuel.2014.10.072.

[29] K. K. Sirkar, Creeping flow mass transfer to a single active sphere in a random spherical inactive particle cloud at high schmidt numbers, Chemical Engineering Science 29 (1974) 863–869. doi:https://doi.org/10.1016/0009-2509(74)80206-X.

[30] O. Desjardins, G. Blanquart, G. Balarac, H. Pitsch, High order conservative finite difference scheme for variable density low Mach number turbulent flows, Journal of Computational Physics 227 (2008) 7125–7159. doi:10.1016/j.jcp.2008.03.027.

[31] J. Capecelatro, O. Desjardins, An Euler–Lagrange strategy for simulating particle-laden flows, Journal of Computational Physics 238 (2013) 1–31. doi:10.1016/j.jcp.2012.12.015.

[32] M. Herrmann, G. Blanquart, V. Raman, Flux Corrected Finite Volume Scheme for Preserving Scalar Boundedness in Reacting Large-Eddy Simulations, AIAA Journal 44 (2006) 2879–2886. doi:10.2514/1.18235.

[33] E. Russo, J. Kuerten, C. van der Geld, B. Geurts, Water droplet condensation and evaporation in turbulent channel flow, Journal of Fluid Mechanics 749 (2014) 666–700. doi:10.1017/jfm.2014.239.

[34] J. Souza, J. Vargas, J. Ordonez, W. Martignoni, O. von Meien, Thermodynamic optimization of fluidized catalytic cracking (FCC) units, International Journal of Heat and Mass Transfer 54 (2011) 1187–1197. doi:10.1016/j.ijheatmasstransfer.2010.10.034.

[35] S. K. Sanjeevi, J. Kuipers, J. T. Padding, Drag, lift and torque correlations for non-spherical particles from Stokes limit to high Reynolds numbers, International Journal of Multiphase Flow 106 (2018) 325–337. doi:10.1016/j.ijmultiphaseflow.2018.05.011.

[36] K. E. Buettner, J. S. Curtis, A. Sarkar, Fluid-particle drag force measurements from particle-resolved CFD simulations of flow past random arrays of ellipsoidal particles, Chemical Engineering Science 235 (2021) 116469. doi:10.1016/j.ces.2021.116469.

[37] M. Zastawny, G. Mallouppas, F. Zhao, B. van Wachem, Derivation of drag and lift force and torque coefficients for non-spherical particles in flows, International Journal of Multiphase Flow 39 (2012) 227–239. doi:10.1016/j.ijmultiphaseflow.2011.09.004.

[38] S. Tenneti, R. Garg, S. Subramaniam, Drag law for monodisperse gas–solid systems using particle-resolved direct numerical simulation of flow past fixed assemblies of spheres, International Journal of Multiphase Flow 37 (2011) 1072–1092. doi:10.1016/j.ijmultiphaseflow.2011.05.010.

[39] P. A. Cundall, O. D. L. Strack, A discrete numerical model for granular assemblies, Géotechnique 29 (1979) 47–65. doi:10.1680/geot.1979.29.1.47, publisher: ICE Publishing.

[40] P. Pepiot, O. Desjardins, Numerical analysis of the dynamics of two- and three-dimensional fluidized bed reactors using an Euler–Lagrange approach, Powder Technology 220 (2012) 104–121. doi:10.1016/j.powtec.2011.09.021.

[41] J. Capecelatro, O. Desjardins, R. Fox, Numerical study of collisional particle dynamics in cluster-induced turbulence, Journal of Fluid Mechanics 747 (2014) R2. doi:10.1017/jfm.2014.194.

[42] M. Al-Sabawi, H. de Lasa, Kinetic modeling of catalytic conversion of methylcyclohexane over USY zeolites: Adsorption and reaction phenomena, AIChE Journal 55 (2009) 1538–1558. doi:10.1002/aic.11825.

[43] R. T. Driessen, S. R. Kersten, D. W. Brilman, A Thiele Modulus Approach for Nonequilibrium Adsorption Processes and Its Application to CO2 Capture, Industrial & Engineering Chemistry Research 59 (2020) 6874–6885. doi:10.1021/acs.iecr.9b05503.

[44] F. B. Wadsworth, J. Vasseur, A. S. Casas, P. Delmelle, K.-U. Hess, P. M. Ayris, D. B. Dingwell, A model for the kinetics of high-temperature reactions between polydisperse volcanic ash and SO2 gas, American Mineralogist 106 (2021) 1319–1332. doi:10.2138/am-2021-7691.

[45] H. Carslaw, J. Jaeger, Conduction of Heat in Solids, 2nd ed., Oxford University Press, Amen House, London, 1959.

Appendix A. Differing Biot Numbers

One of the limitations of the present approach is the inability to accurately handle different Biot numbers across species. In this section we will discuss why it is difficult (or impossible) to use this approach with Biot numbers that vary across species; a linear decoupling of the type discussed in Sec. 2.1 may not be possible in this case. Begin by taking the approach of Sec. 2.2 from Eq. (6) without the assumption that Biot numbers are equal for all species. For the type of method proposed here, $\hat{Y}_k$ must be written as some linear combination of reference solutions, each of which must be a solution to Eq. (8) for λ_k. The equation

$$\hat{Y}_k = \sum_j \alpha_{k,j} \hat{Z}^{(\lambda_k, b_j)} \tag{A.1}$$

then needs to satisfy Eq. (6). For a representation of this form to exist, it needs to be possible to find coefficients $\alpha_{j,k}$ such that the left side of Eq. (6) is constant on the boundary. Here, instead of letting Bi be a scalar, let Bi be the matrix with Biot numbers for each species Bi_1, Bi_2, $\ldots$, Bi_{N_r} on the diagonal ($\mathrm{Bi} = \mathrm{Diag}_i(\mathrm{Bi}_i)$). First, observe

$$\begin{aligned}
&(\mathrm{Bi}^{-1}(\nabla \boldsymbol{Y} \cdot \mathbf{n}) + R\boldsymbol{Y})_i \\
&\quad = (\mathrm{Bi}^{-1} R^{-1} (\nabla \hat{\boldsymbol{Y}} \cdot \mathbf{n}) + R^{-1} \hat{\boldsymbol{Y}})_i \\
&\quad = \frac{1}{\mathrm{Bi}_i} \sum_k l_{i,k} (\nabla \hat{Y}_k \cdot \mathbf{n}) + \sum_k l_{i,k} \hat{Y}_k \\
&\quad = \frac{1}{\mathrm{Bi}_i} \sum_{k,j} l_{i,k} \alpha_{k,j} (\nabla \hat{Z}^{(\lambda_k, b_j)} \cdot \mathbf{n}) + \sum_{k,j} l_{i,k} \alpha_{k,j} \hat{Z}^{(\lambda_k, b_j)} \\
&\quad = \sum_{k,j} l_{i,k} \alpha_{k,j} \frac{b_j}{\mathrm{Bi}_i} \left(1 - \hat{Z}^{(\lambda_k, b_j)}\right) + \sum_{k,j} l_{i,k} \alpha_{k,j} \hat{Z}^{(\lambda_k, b_j)} \\
&\quad = \underbrace{\sum_{k,j} l_{i,k} \alpha_{k,j} \frac{b_j}{\mathrm{Bi}_i}}_{S_i} + \underbrace{\sum_{k,j} l_{i,k} \alpha_{k,j} \left(1 - \frac{b_j}{\mathrm{Bi}_i}\right) \hat{Z}^{(\lambda_k, b_j)}}_{T_i}.
\end{aligned}$$

For this quantity to be constant, we must find a sequence (b_j) such that S_i and T_i are constant. As long as S_i converges (as is the case when it is a finite sum), it is constant. T_i is made constant in the case of all equal Biot numbers by taking $b_j = \mathrm{Bi}_j$ so that $T_i = 0$. In the case of non-equal Biot numbers, it is not clear how $\alpha_{k,j}$ and b_j may be chosen, nor if it is possible for them to be chosen. In the case in which (b_j) is an infinite sequence, this truncation will introduce an additional source of error.